New 10-Layer Hexagonal Perovskites: Relationship between Cation and Vacancy Ordering and Microwave Dielectric Loss

P. Mallinson,[†] J. B. Claridge,[†] D. Iddles,[‡] T. Price,[‡] R. M. Ibberson,[§] M. Allix,[†] and M. J. Rosseinsky*,[†]

Department of Chemistry, The University of Liverpool, Liverpool L69 7ZD, U.K., ISIS Facility, CCLRC - Rutherford Appleton Laboratory, Chilton, Didcot, Oxon., OX11 0QX, U.K., and Ceramics Division, Filtronic Comtek, Enterprise Drive, Station Road, Four Ashes, Wolverhampton WV10 7DB, U.K.

Received July 15, 2006. Revised Manuscript Received September 28, 2006

The new ceramic materials $Ba_{10}Mg_{0.25}Ta_{7.9}O_{30}$ and $Ba_{10}Co_{0.25}Ta_{7.9}O_{30}$ have been synthesized in isolation and their dielectric and crystallographic properties characterized fully. The crystal structure determination, using a combination of X-ray and neutron powder diffraction and electron microscopy, reveals a 10-layer perovskite structure that involves the $(hcccc)_2$ stacking sequence with a pair of face-sharing octahedral sites separating three layers of corner-sharing octahedra. The structure is discussed in comparison with the related eight-layer $Ba_8ZnTa_6O_{24}$, which involves the $(hccc)_2$ stacking sequence, discovered in an earlier study. The microwave dielectric properties of both materials are determined ($Ba_{10}Mg_{0.25}Ta_{7.9}O_{30}$ Qf = 33 585 at 4.02 GHz, $\epsilon_r = 28$, and a temperature coefficient of resonant frequency $\tau_f = 30.2$ ppm/°C; $Ba_{10}Co_{0.25}Ta_{7.9}O_{30}$ Qf = 36 693 at 3.78 GHz, $\epsilon_r = 30$, $\tau_f = 28.6$ ppm/°C), and factors controlling dielectric behavior in hexagonal perovskites are identified from the available structural and property data.

Introduction

Base stations in mobile telecommunications networks currently require transition metal oxide ceramics as filter and resonator components.[1] There is thus a need for new materials with enhanced figures of merit for this application and for an enhanced understanding of the structure−property−composition relationships governing the behavior of this class of materials.[2] The materials requirements are diverse and to some extent conflicting—a high relative permittivity ϵ_r is required as device dimension scales as $(\epsilon_r)^{-1/2}$, but the dielectric loss (tan δ or Q^{-1}) needs to be minimized to retain maximal frequency resolution.[3] It is observed that the loss increases with increasing permittivity. A further requirement is the control of the temperature coefficient of the resonant frequency τ_f to within the range of ±10 ppm. In order to maximize the permittivity and minimize the loss, attention has focused on complex oxides containing transition metals in oxidation states with d^0 electronic configurations such as Ti^{4+}, Ta^{5+}, and Nb^{5+}. For applications at 2 GHz, the optimal material is the perovskite $Ba_3ZnTa_2O_9$[2,4,5] suitably doped in order to minimize τ_f, though the system is difficult to process due to the complex requirements for the control of cation order and composition to attain the required figures of merit. Attention has thus recently focused on other structure types. The related class of hexagonal perovskites which involve both cubic (ABC) and hexagonal (ABA) stacking of close-packed BaO_3 layers have attracted attention recently.[6−8] The key structural difference is the occurrence of face-sharing octahedra within the ABA hexagonal parts of the structure in addition to the familiar cubic perovskite corner-sharing in the ABC parts. These systems have enhanced compositional flexibility with respect to the perovskites, due to their ability to accommodate B-site cation vacancies on the face-sharing sites within the ABA sections of the structure. There are two nomenclatures in common usage to describe the stacking sequences in these mixed hexagonal-cubic systems. An AO_3 layer (layer B in the three letter sequences which follow) is described as h if its two neighboring layers are the same (i.e., it is the middle layer in an ABA sequence) or c if they are different (i.e., it is the middle layer in an ABC sequence). Hexagonal perovskites can be further characterized as "twin" or "shift" structures[9] depending on whether one (twin) or two (shift) hexagonal layers occur together in the structure.

Zn loss from $Ba_3ZnTa_2O_9$ leads to the formation of $Ba_8ZnTa_6O_{24}$ (Figure 1a) with a $(hccc)_2$ stacking sequence.[10,11] The 8-layer $Ba_8ZnTa_6O_{24}$ ("twin" $(hccc)_2$)[10] and related

[†] The University of Liverpool.
[‡] Filtronic Comtek.
[§] CCLRC - Rutherford Appleton Laboratory.

(1) Reaney, I. M.; Iddles, D. *J. Am. Ceram. Soc.* **2006**, *89*, 2063.
(2) Davies, P. K.; Tong, J.; Negas, T. *J. Am. Ceram. Soc.* **1997**, *80*, 1727−1740.
(3) Vanderah, T. A. *Science* **2002**, *298*, 1182−1184.
(4) Desu, S.; O'Bryan, H. M. *J. Am. Ceram. Soc.* **1985**, *68*, 546−551.
(5) Kawashima, S.; Nishida, M.; Ueda, I.; Ouchi, H. *J. Am. Ceram. Soc.* **1983**, *66*, 421−423.
(6) Rawal, R.; Feteira, A.; Hyatt, N. C.; Sinclair, D. C.; Sarma, K.; Alford, N. M. *J. Am. Ceram. Soc.* **2006**, *89*, 332−335.
(7) Troillard, G.; Teneze, N.; Boullay, P.; Mercurio, D. *J. Solid State Chem.* **2004**, *177*, 1188−1196.
(8) Vanderah, T. A.; Miller, V. L.; Levin, I.; Bell, S. M.; Negas, T. *J. Solid State Chem.* **2004**, *177*, 2023−2038.
(9) Trolliard, G.; Teneze, N.; Boullay, P.; Mercurio, D. *J. Solid State Chem.* **2004**, *177*, 1188−1196.
(10) Moussa, S. M.; Claridge, J. B.; Ibberson, R. M.; Rosseinsky, M. J.; Clarke, S.; Iddles, D.; Price, T.; Sinclair, D. C. *Appl. Phys. Let.* **2003**, *82*, 4537−4539.
(11) Thirumal, M.; Davies, P. K. *J. Am. Ceram. Soc.* **2005**, *88*, 2126−2128.

10.1021/cm0616477 CCC: $33.50
Published on Web 11/30/2006

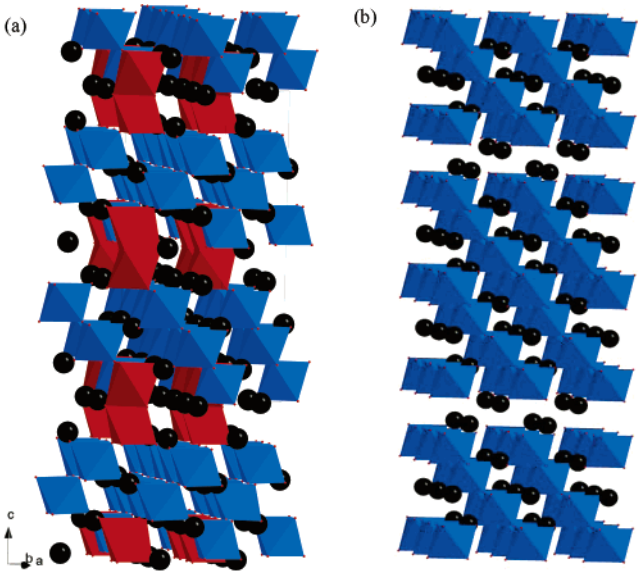

Figure 1. Two distinct types of hexagonal perovskite stacking sequences for $A_8B_{8-x}O_{24}$. (a) The 8-layer "twin"-type structure. The face-sharing octahedra in the h layer are distinguished by shading in red. (b) The 8-layer "shift"-type structure. The two adjacent h layers produce a vacant layer of octahedral sites. The A site cations are represented as black spheres, B sites as anion coordination octahedra.

$Ba_8CoNb_6O_{24}$ ("shift" (ccchhccc))[12] (Figure 1b) systems both display interesting figures of merit and less complex processing than pseudo-cubic BZT. For example, $Ba_8ZnTa_6O_{24}$ has a Qf value of 68000 GHz, ascribed to the ordering of both lower-charged Zn^{2+} cations and B-site vacancies within the hexagonal regions of the structure. In contrast, the shift-structure titanate materials in the $Ba_nLa_4Ti_{3+n}O_{12+3n}$ series have higher permittivities but enhanced losses compared to the tantalates and niobates.[13] An interesting aspect of the titanate series is the ability to synthesize homologous sequences with varying thicknesses of cubic layer between the hexagonal sections of the structure.

The aim of this work is to achieve the same stacking sequence control of the separation between the h layers in the "twin"-type structures. The study is motivated in part by the observation that $Ba_8ZnTa_6O_{24}$ cannot be synthesized without a small concentration of a second phase which was identified by X-ray and electron diffraction as a 10-layer analogue of the 8-layer material.[10] In this paper we report the search for 10-layer materials with Zn^{2+}, Co^{2+}, and Mg^{2+} on the octahedral sites, the isolation of the 10-layer tantalate structure, and the crystallographic, microwave dielectric, and microstructural characterization of resonators derived from it. The refined structure is discussed together with that of the parent 8-layer phase $Ba_8ZnTa_6O_{24}$ which was not reported in detail in the original communication.

Experimental Section

The Ba−Zn−Ta−O, Ba−Mg−Ta−O, and Ba−Co−Ta−O phase fields were investigated by solid-state reaction of $BaCO_3$ (Solvay, 99%+), Ta_2O_5 (Starck, 99%+), MgO (Sigma-Aldrich, 99.999%), Co_3O_4 (Sigma-Aldrich, 99.99%), and ZnO (Alfa-Aesar, 99.99%) powders initially calcined at 1200 °C for 4 h, reground, and pressed into a pellet before reaction at temperatures between 1400 and 1600 °C for 12−36 h in alumina crucibles. Similar reactions were carried out for analogous niobates, using Nb_2O_5 (Sigma-Aldrich, 99.9%) as the starting material.

Resonators for microwave dielectric characterization were prepared from stoichiometric amounts of $BaCO_3$, Ta_2O_5, and dried MgO/ZnO ball-milled in a HDPE bottle with water and zirconia stabilized MgO media for 16 h. The sample was dried, sieved (0.25 mm mesh), and then calcined at 1200 °C for 4 h. A total of 2 wt % of polyethylene glycol was added as a binder, and the sample was ball-milled for a further 16 h before being dried ready for use. Resonators were fired at temperatures between 1500 and 1650 °C.

Synthesis of the $Ba_8ZnTa_6O_{24}$ sample and details of powder neutron and X-ray data collection are given in the earlier report.[10]

Powder X-ray diffraction data were collected on a Panalytical X-Pert diffractometer with Co $K\alpha_1$ radiation in Bragg−Brentano geometry to assess phase purity and sample quality during processing. As Rietveld refinement of these data consistently indicated a high level of preferred orientation, data for structural analysis of $Ba_{10}Mg_{0.25}Ta_{7.9}O_{30}$ were collected in capillary transmission geometry on station 9.1 of the Synchrotron Radiation Source (SRS) at Daresbury Laboratory with the sample diluted in a 1:1 ratio with amorphous boron contained in a 0.5 mm diameter capillary, at a wavelength of 0.950048 Å. Neutron powder diffraction data were collected on the high-resolution powder diffractometer HRPD at the ISIS Facility, Rutherford Appleton Laboratory. Data were refined by the Rietveld method using the GSAS software package.[14] Inspection of the difference Fourier map from the final refined model did not lead to the identification of extra sites or problems with the model.

Samples for transmission electron microscopy were prepared by crushing the powder in *n*-butanol, and the small crystallites in suspension were deposited onto a holey carbon film, supported by a copper grid. The electron diffraction (ED) study was carried out with a JEOL 2000FX electron microscope. Energy dispersive spectroscopy (EDS) analyses were systematically carried out during the ED study, the JEOL 2000FX being equipped with an EDAX analyzer.

Scanning electron microscopy was performed on a Hitachi S-2460N SEM in backscattering mode on pellets cross-sectioned with a diamond saw.

The microwave measurements were carried out with samples supported on alumina at 3.82−4.04 GHz in a silver-plated 90 mm cubic cavity: Q was determined directly from reflection measurements and ϵ_r calculated from the resonant frequency and sample dimensions, using the techniques established by Hakki, Coleman et al.[15−17] τ_f was calculated from measurement of the resonant frequency between −10 °C and 60 °C.

Results

Isolation and Compositional Characterization of 10-Layer Phases. The target 10-layer type structure was first identified during attempts to synthesize the Mg-containing 8-layer phase $Ba_8MgTa_6O_{24}$. At this composition with firings of 1400−1600 °C for 12−36 h, the 8-layer structure was not identified in any of the XRD patterns. At 1400 °C the product was a mixture of $Ba_3MgTa_2O_9$ and $Ba_5Ta_4O_{15}$; as

(12) Mallinson, P. M.; Allix, M. M. B.; Claridge, J. B.; Ibberson, R. M.; Iddles, D. M.; Price, T.; Rosseinsky, M. J. *Angew. Chem. Int. Ed.* **2005**, *44*, 7733−7736.
(13) Okawa, T.; Kiuchi, K.; Okabe, H.; Ohsato, H. *Ferroelectrics* **2002**, *272*, 2337−2342.
(14) Larson, A. C.; von Dreele, R. B. *General Structure Analysis System (GSAS)*, Los Alamos National Laboratory Report LAUR 86-748, 2004.
(15) Hakki, B. W.; Coleman, P. D. *IRE Trans MTT* **1960**, *8*, 402−410.
(16) Courtney, W. E. *IEEE Trans MTT* **1970**, *8*, 476−485.
(17) Hennings, D.; Schnabel, P. *Philips J. Res.* **1983**, *38*, 295−311.

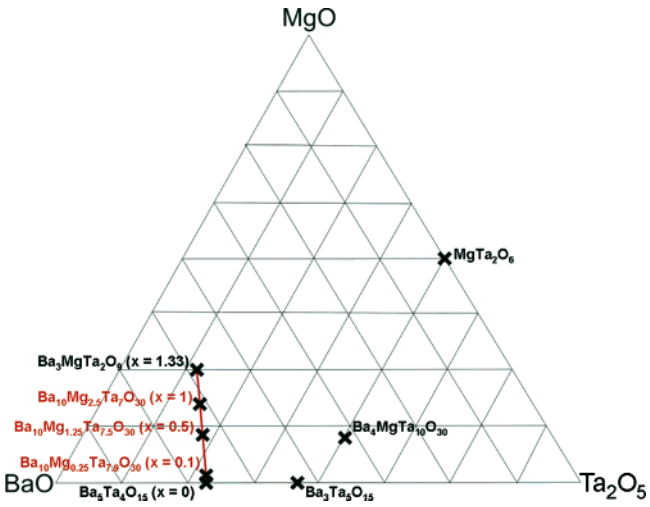

Figure 2. Selected phases in the system Ba−Ta−Mg−O. Previously identified phases reported in the ICSD and JCPDS database are shown in black with possible 10-layer compositions with the general formula $Ba_{10}Mg_{2.5x}Ta_{8-x}O_{30}$ in red. Further ternary phases identified but not shown on the figure are $Ba_2Ta_{15}O_{32}$, $BaTa_2O_6$, $Ba_7Ta_6O_{16}$, $Ba_4Ta_2O_9$, $Ba_3Ta_2O_8$, $Ba_6Ta_2O_{11}$, $BaTa_4O_{11}$, $Ba_{5.5}Ta_{21.8}O_{60}$, and $Mg_4Ta_2O_9$.

the temperature was increased to 1450 °C, the amount of $Ba_5Ta_4O_{15}$ was reduced and a hexagonal phase with similar in-plane *a*-*b* lattice parameters to the eight layer phase but an enlarged *c* lattice parameter was observed. The 23 Å *c* parameter derived from powder X-ray data recorded on this sample indicates the presence of 10 BaO_3 layers in the stacking sequence. Further increases in reaction temperature gave samples containing solely the 10-layer phase and $Ba_3MgTa_2O_9$.

A 10-layer hexagonal perovskite structure would have the general formula $Ba_{10}Mg_{2.5x}Ta_{8-x}O_{30}$, where $x = 0-1.333$ (Figure 2). Synthesis of single-phase samples was attempted with $x = 1$, 0.667, 0.4, 0.2, and 0.1. The $x = 1$ ($Ba_{10}Mg_{2.5}Ta_7O_{30}$) composition gave a product that was mainly $Ba_3MgTa_2O_9$ with only a small amount of the 10-layer phase with a firing at 1550 °C for 12 h. The $x = 0.1$ composition ($Ba_{10}Mg_{0.25}Ta_{7.9}O_{30}$) affords a single-phase 10-layer product, obtained with a firing of 1550 °C for 12 h. Firing at 1450 °C for 12 h gave no 10-layer phase, only a mixture of $Ba_3MgTa_2O_9$ and $Ba_5Ta_4O_{15}$, showing that the 10-layer phase is stable only at high temperature and in a narrow composition window. The pure $x = 0.1$ 10-layer phase decomposes to $Ba_3MgTa_2O_9$ and $Ba_5Ta_4O_{15}$ on annealing at both 1300 °C and 1400 °C, and then reforms as a pure phase at 1550 °C, demonstrating that this is truly a high-temperature phase. The same $x = 0.1$ composition was stable for Co in place of Mg, although in this case the 8-layer $Ba_8CoTa_6O_{24}$ is the competing impurity phase rather than the cubic perovskite observed in the Mg case.

As the 10-layer phase had originally been identified in the Zn 8-layer sample,[10] attempts were made to isolate a zinc-containing 10-layer phase following the successful isolation of the Co and Mg analogues. After identifying the correct 10-layer composition within the family $Ba_{10}M^{2+}{}_{2.5x}Ta_{8-x}O_{30}$ as $x = 0.1$, further attempts were made to synthesize $Ba_{10}Zn_{0.25}Ta_{7.9}O_{30}$. Firing at 1500 °C for 12 h did produce a sample containing a 10-layer phase but also present were $Ba_8ZnTa_6O_{24}$, $Ba_5Ta_4O_{15}$, and a tetragonal tungsten bronze (TTB) type phase related to $Ba_3Ta_5O_{15}$. Firing for another 12 h at 1500 °C removed the $Ba_8ZnTa_6O_{24}$ impurity but increased the amount of $Ba_5Ta_4O_{15}$, ascribed to Zn loss from the sample. Firing at 1400 °C for 12 h produced no 10-layer material but mainly $Ba_5Ta_4O_{15}$ with some $Ba_8ZnTa_6O_{24}$ and the TTB. Re-firing this sample at 1550 °C for 12 h resulted in some 10-layer compound being formed, but the sample still contained significant amounts of $Ba_5Ta_4O_{15}$. Another 12 h firing at 1550 °C led to an almost pure phase of $Ba_5Ta_4O_{15}$. Increasing the reaction temperature further to 1600 °C led to the sample melting. Firing at 1400 °C for 62 h and 164 h gave a mix of the 10-layer phase and $Ba_5Ta_4O_{15}$, with more of the impurity from the longer firing. Thus within the range of compositions and reaction conditions studied here, it was not possible to isolate a sufficiently pure sample of the 10-layer zinc phase for measurement of the dielectric properties, although the existence of this phase, initially suggested in reference 10 is confirmed.

Attempts to make the niobate analogues of the 10-layer phases identified above proved unsuccessful with firings between 1300 and 1550 °C. The products of the reaction in every case were a mixture of $Ba_5Nb_4O_{15}$ and $Ba_3MNb_2O_9$ ($M = Mg^{2+}$, Co^{2+}, and Zn^{2+}).

The low divalent metal content in the compositions $Ba_{10}Mg_{0.25}Ta_{7.9}O_{30}$ and $Ba_{10}Co_{0.25}Ta_{7.9}O_{30}$ requires direct confirmation that all three elements are present in the same oxide phase. Analysis of a number of individual grains of the 10-layer Mg/Ta phase by EDS in the TEM showed the sample to be homogeneous and gave a metal composition $Ba_{10}Mg_{0.83(8)}Ta_{7.59(38)}$. The significant point here is that the Ba/Ta ratio is confirmed. Given the low Mg loading and relative insensitivity of EDS to lighter elements, the EDS qualitatively confirms the incorporation of Mg in the 10-layer phase, with a level of quantitative agreement that is reasonable. The 10-layer structure adopted by $Ba_{10}Mg_{0.25}Ta_{7.9}O_{30}$ and $Ba_{10}Co_{0.25}Ta_{7.9}O_{30}$ involves the $(hcccc)_2$ "twin" stacking sequence with a pair of face-sharing octahedral sites separating three layers of corner-sharing octahedra (Figure 3a).

Diffraction Characterization of the 10-Layer Structures. Neutron diffraction data suggests that the Mg and Co analogues are isostructural with lattice parameters $a = 5.810524(8)$ Å, $c = 23.88460(6)$ Å, and $a = 5.812204(12)$ Å, $c = 23.896418(90)$ Å, respectively. However profile analysis of the $Ba_{10}Co_{0.25}Ta_{7.9}O_{30}$ data revealed an anomalous peak shape, the origin of which is still to be established. At this stage therefore the detailed discussion of the 10-layer structure is confined to that adopted by $Ba_{10}Mg_{0.25}Ta_{7.9}O_{30}$. Data collection details are given in Table 1.

The distribution of cations and vacancies within the 10-layer structure is complex and exerts a controlling influence on the microwave dielectric properties. There are two distinct space groups which can describe the 10-layer structure within the $a = 5.810524(8)$ Å basal plane cell parameters—it is important to note that both X-ray and neutron diffraction data indicate that the basal plane unit cell parameters reduced by $\sqrt{3}$ compared with the 8-layer compound. In the centric $P6_3/mmc$ space group, there is a mirror plane containing the three oxygen anions which form the shared face of the h-layer octahedra, whereas in noncentric $P6_3mc$ this symmetry

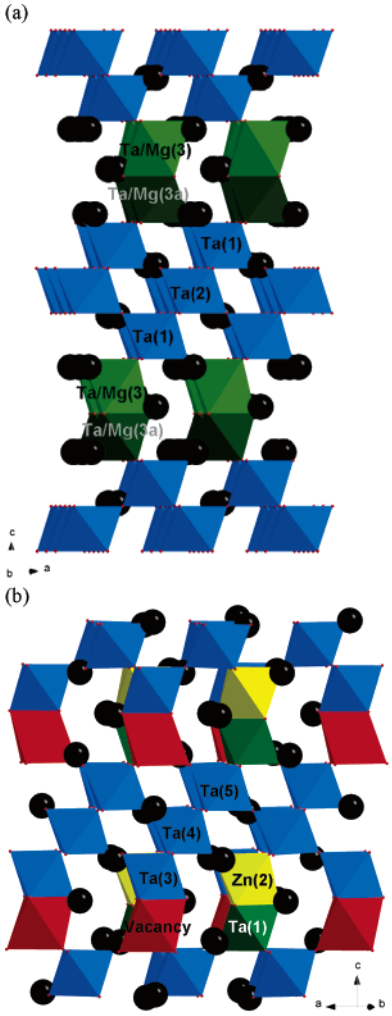

Figure 3. Structures of the 10- and 8-layer members of the Ba−M−Ta−O hexagonal perovskite series—corner-sharing octahedra are shown in blue, with the crystallographically distinct sites in the face-sharing layers distinguished by other colors. The larger number of crystallographically distinct sites in the 8-layer structure arises from more extensive cation and vacancy ordering. (a) The 10-layer structure of $Ba_{10}Mg_{0.25}Ta_{7.9}O_{30}$ with two symmetry-independent face-sharing octahedral sites. (b) The 8-layer structure of $Ba_8ZnTa_6O_{24}$ with three symmetry-independent face-sharing octahedral sites.

Table 1. Refinement and Data Collection Details for Powder X-ray and Neutron Diffraction Data for $Ba_{10}Mg_{0.25}Ta_{7.9}O_{30}$[a]

	X-ray	neutron
λ (Å)	0.950027(5)	1.37−4.89 (35−125 ms)
no. of profile points	4200	12482
2θ range (deg), step	8−50, 0.01	⟨168⟩
d-spacing range (Å)	1.13−6.80	0.73−2.53
excluded regions	0	0
χ^2	1.27	2.28
R_E (%)	3.80	6.12
R_{wp} (%)	4.28	9.24
R_p (%)	3.40	7.09

[a] For the two-histogram refinement combined $R_E = 4.89\%$, $R_{wp} = 6.80\%$, $R_p = 3.41\%$; $\chi^2 = 1.919$ for 77 variables.

element is absent and the two face-sharing octahedral sites are symmetry-inequivalent. Refinement of the neutron powder diffraction data clearly shows that the noncentric space group $P6_3mc$ ($\chi^2 = 2.539$, $R_p = 8.19$, $R(F^2) = 10.78$) is favored over the centric space group $P6_3/mmc$ ($\chi^2 = 3.187$, $R_p = 8.88$, $R(F^2) = 13.23$). The identification of the atoms in the refined structure (Table 2) indicates species initially related by a center of symmetry by the addition of the "a" suffix, e.g., Ba(3) and Ba(3a). The degree of pseudosymmetry in the structure required some care in the performance of the Rietveld refinement in the noncentric symmetry—this was particularly the case for the center-related O(3) and O(3a) atoms which differ only by 5−10 esd's in their bond lengths to neighboring atoms. The atoms were refined with 90% damping of the shifts in the least-squares cycles initially—once a stable refinement had converged, this damping was released. Refinement with all atoms of the same type constrained to have the same displacement parameter converges to $\chi^2 = 2.43$—relaxation of this constraint reduces χ^2 to 2.18 but gives a large spread in refined values of the displacement parameter. In order to investigate the origin of this spread in displacement parameters, a trial anisotropic refinement was carried out, showing that Ba(3a) has the largest U and is elongated within the *ab* plane. This indicated static disorder in the location of Ba(3a), which was displaced onto the *x-xz* position. This allowed convergence to $\chi^2 = 2.29$ with the physically sensible constraint applied to all the isotropic temperature factors. Application of an equivalent disordered displacement to the pseudosymmetry-related Ba(3) site did not affect χ^2, and thus these two sites are now clearly inequivalent in the refined structure. This displacement thus removes the centric pseudosymmetry, as indicated by the ADDSYM routine within the PLATON suite of software.[18] At this stage of the analysis, the refined structure revealed that Ba(3a) was significantly overbonded (BVS 2.87) primarily due to a short, 2.387(6) Å, bond to O(1). Ta(3) was also found to be significantly underbonded (BVS 2.98). A trial structure in which anisotropic displacement parameters for O(1) were refined showed an elongated distribution of scattering density implying a split oxygen site in line with the static disorder modeled for Ba(3a) and described above. Accordingly a new atom position, O(1′), displaced some 0.5 Å further from Ba(3a) than O(1), was introduced to the structural model. The coordination environments around Ba(3a) and the face-sharing sites are shown in Figure 4. The atomic coordinates of O(1′) and isotropic displacement parameters for both O(1) and O(1′) were refined. Models with the site occupancy for O(1) and O(1′) fixed at 2/3 and 1/3, respectively, mirroring the static disorder at Ba(3a) and freely refined were tested. In each case convergence was achieved with $\chi^2 = 1.93$. The O(1′) occupancy refined to 0.48(2), illustrating the limits of sensitivity to this aspect of the model, and so was fixed at 1/3 in the following refinements. Details of data collection and the structure refinement are given in Tables 1 and 2. The final profile fits to the neutron and synchrotron data are shown in Figure 5. Bond lengths and angles are given in Table 3. The bond valence sums for this model are given in Table 4. They show that the over-bonding at Ba(3a) is resolved by the local correlation of Ba(3a) and O(1′) occupancy. With a split site O(1):O(1′) occupancy of 2/3:1/3 the BVS of the Ta(3) and Ta(3a) sites are significantly different from the ideal values (3.223 and 4.354, respectively). However, if it is assumed that when the Ta(3) site is occupied the O(1′) site is fully occupied the BVS is then a

(18) Spek, A. L. *Acta. Crysallogr.* **1990**, A46, C34.

Table 2. Structural Parameters for $Ba_{10}Mg_{0.25}Ta_{7.9}O_{30}$ Refined against HRPD Powder Neutron Diffraction and Synchrotron X-ray Data[a]

atom	multiplicity	*x/a*	*y/b*	*z/c*	occupancy	*U* (Å^2)
Ba(1)	2	0.33333	0.66667	0.7568(5)	1	0.0074(3)
Ba(2)	2	0.33333	0.66667	0.4508(3)	1	0.0074(3)
Ba(2a)	2	0.33333	0.66667	0.0586(4)	1	0.0074(3)
Ba(3)	2	0	0	0.8415(2)	1	0.0074(3)
Ba(3a)	6	0.0296(4)	−0.0296(4)	0.1634(3)	0.33333	0.0074(3)
Ta(1)	2	0	0	0.0059(3)	1	0.0050(2)
Ta(2)	2	0.33333	0.66667	0.9059(3)	1	0.0050(2)
Ta(2a)	2	0.33333	0.66667	0.6081(3)	1	0.0050(2)
Mg(3)	2	0.33333	0.66667	0.3030(5)	0.0625	0.0057(5)
Ta(3)	2	0.33333	0.66667	0.3030(5)	0.348(12)	0.0057(5)
Mg(3a)	2	0.33333	0.66667	0.2072(3)	0.0625	0.0057(5)
Ta(3a)	2	0.33333	0.66667	0.2072(3)	0.602(12)	0.0057(5)
O(1)	6	0.1676(7)	0.8324(7)	0.2431(6)	0.66667	0.0105(1)
O(1′)	6	0.1738(8)	0.8262(8)	0.2633(6)	0.33333	0.0105(1)
O(2)	6	0.4889(2)	0.5111(2)	0.8623(2)	1	0.0105(1)
O(2a)	6	0.5016(3)	0.4984(3)	0.1494(6)	1	0.0105(1)
O(3)	6	0.1653(3)	0.8347(3)	0.9587(2)	1	0.0105(1)
O(3a)	6	0.833405(4)	0.166594(4)	0.05262(2)	1	0.0105(1)

[a] Lattice constants: $a = 5.810529(7)$ Å, $c = 23.884602(52)$ Å; $V_c = 698.361(2)$ Å^3. Space group: $P6_3mc$. $Z = 1$.

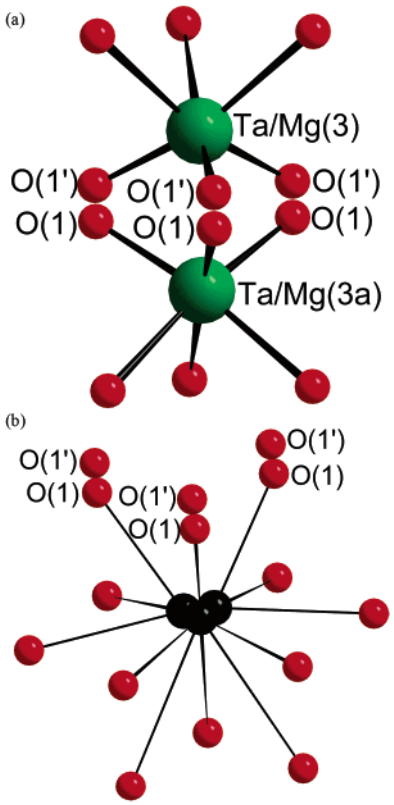

Figure 4. Disordered sites in $Ba_{10}Mg_{0.25}Ta_{7.5}O_{30}$. (a) Coordination around the Ta/Mg(3) and Ta/Mg(3a) sites showing the split O(1)/O(1′) positions. (b) Coordination around Ba(3a) showing the 3-fold disorder of Ba(3a) and the split O(1)/O(1′) positions. The occupancies of the O(1) and O(1′) positions are 2/3 and 1/3, respectively.

reasonable 4.606. The same assumption with the Ta(3a) and O(1) sites also improves the Ta(3a) bond valence to 4.855.

This model has the Mg cations equally distributed over the face-sharing Ta(3) and Ta(3a) sites, as refinement of the site occupancies and inspection of the bond valence sums indicates that all the corner-sharing octahedral sites (Ta(1), Ta(2), and Ta(2a)) are occupied solely by Ta(V). Refining the Mg occupancy on the face-sharing sites showed it to have a preference for the 3 site over the 3a. The presence of Mg on the 3 site is supported by the bond valence sums (Table 4); this shows Mg(3) with 2.237 and Mg(3a) with 2.400. However, due to the low density of Mg (only 0.0625 fractional occupancy when split equally) over the two sites, the limited improvement in the fit parameters seen, and with the small difference in the bond valence, it is impossible to conclusively state ordering of the Mg onto the 3 site. The Ta occupations on the face-sharing sites were refined with the constraint to keep the total composition correct. This lowered χ^2 to 1.937 from 1.943 seen with equal Ta distribution. The Ta showed a preference for the 3a site over the 3 site with the occupations 0.602(12) and 0.348(12), respectively.

The unit cells of the 10-layer phases $Ba_{10}Mg_{0.25}Ta_{7.9}O_{30}$ and $Ba_{10}Co_{0.25}Ta_{7.9}O_{30}$ are smaller (by a factor of $\sqrt{3}$) in the *xy* plane than that of the 8-layer compound $Ba_8ZnTa_6O_{24}$ because there is a reduced extent of cation and vacancy ordering within the face-sharing pairs of octahedral sites. There are two crystallographically distinct face-sharing octahedral sites in the 10-layer structure. The structure refined from the Bragg peaks does not fully explain the observations in the 110 zone electron diffraction patterns (Figure 6) of rods of scattering passing through the positions where superstructure reflections due to the cation ordering found in the 8-layer phase are expected. This is attributed to the existence of local cation and vacancy order within discrete pairs of h layers but not correlated from one pair of h layers to another. It is reasonable to suggest that the local ordering pattern may be related to that observed for the 8-layer phase $Ba_8ZnTa_6O_{24}$, which has a larger number of crystallographically inequivalent sites in the pair of face-sharing octahedral layers and thus it is appropriate at this point to discuss the structure of this material.

Structure of the 8-Layer Material. The initial report of the parent 8-layer phase $Ba_8ZnTa_6O_{24}$ contained a brief description of the structure,[10] but the complexity of the vacancy distribution merits further discussion here. Details of data collection are given in Table 5, with refined parameters given in Table 6 and bond lengths in Table 7. The *ab* cell parameters are expanded by $\sqrt{3}$ compared with the 10-layer material due to positional ordering of the vacancies onto specific face-sharing octahedral sites in the "h" part of the stacking sequence. The ordering of the face-sharing octahedral cation vacancies thus lowers the symmetry

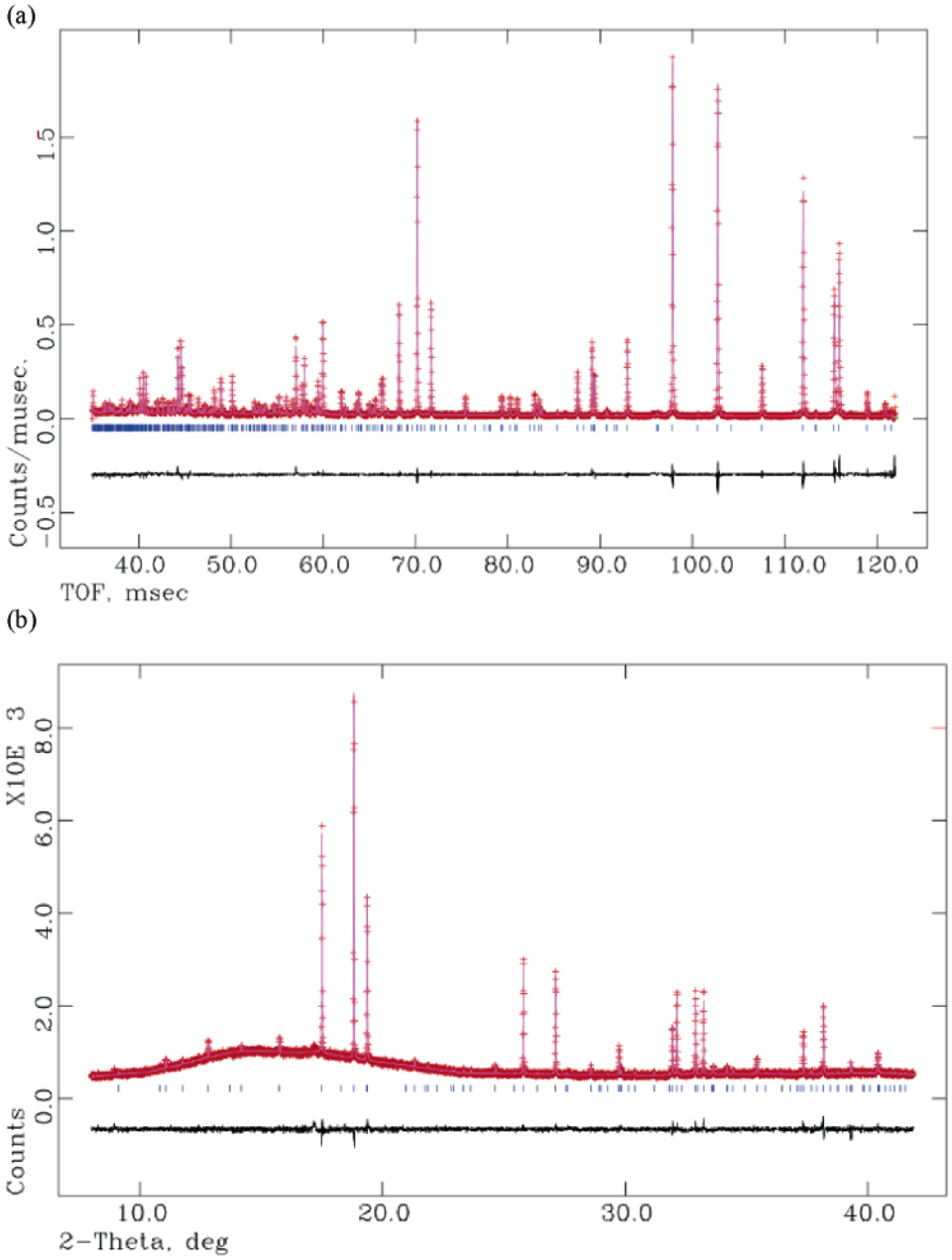

Figure 5. Observed, calculated, and difference plots from Rietveld refinement of neutron and X-ray powder diffraction data for $Ba_{10}Mg_{0.25}Ta_{7.5}O_{30}$ (a) Neutron (HRPD, ISIS). (b) Synchrotron X-ray (Daresbury SRS, station 9.1). Observed data are shown as crosses, and the calculated fit to the data is represented as a solid line, with the difference between the observed and calculated intensity shown below. Tick marks represent the positions of the Bragg reflections. Data collection details are given in Table 1 and refined parameters in Table 2.

from $P6_3/mmc$ (a = 5.82144 Å, c = 19.06594 Å) to $P6_3/mcm$ (a = 10.08304 Å, c = 19.0659 Å). Refinement indicates that complete ordering of the vacancies occurs with further lowering of the symmetry to the noncentric space group $P6_3cm$ identified for $Ba_8NiTa_6O_{24}$.[19] The combined X-ray and neutron refinement demonstrates that all the corner-sharing octahedra are completely occupied by Ta cations with the lower charged Zn cations and the vacancies being located on the face-sharing sites: the 0,0,0 2a site is entirely vacant. The enlarged cell in the xy plane compared with $Ba_{10}Mg_{0.25}Ta_{7.9}O_{30}$ arises because the long-range vacancy and cation ordering within the bilayer of face-sharing octahedra. The two layers of face-sharing octahedra consist of a layer of Ta(3) (100% Ta) and Zn(2) (75% Zn, 4.8(9)% Ta) and a layer of vacant sites and Ta(1) (85.3(8)% Ta). There are two distinct sites in the corner-sharing layers, both of which are 100% occupied by Ta−Ta(4), which is connected by oxide anions to the layer containing the Zn(2) and 100% Ta Ta(3) site, and Ta(5) connected to the layer containing Ta(1) and the vacant site.

The refined composition of $Ba_8ZnTa_{5.88(6)}O_{24}$ is consistent with the ideal $Ba_8ZnTa_6O_{24}$ composition within 2σ, although the data are of insufficient quality to the rule out a small level of accompanying Ta and O vacancies. The refined bond lengths at the Ta and Zn sites thus reflect the detailed structural response to the vacancy and site ordering in a chemically sensible manner.

(19) Abakumov, A. M.; van Tendeloo, G.; Scheglov, A. A.; Shpanchenko, R. V.; Antipov, E. V. *J. Solid State Chem.* **1996**, *125*, 102−107.

Table 3. Interatomic Distances for $Ba_{10}Mg_{0.25}Ta_{7.9}O_{30}$

		distance, Å			distance, Å
×6	Ba(1)−O(1)	2.924 (5)	×3	Ba(2)−O(2)	2.767 (6)
×3	Ba(1)−O(2)	2.97 (1)	×6	Ba(2)−O(3)	2.911 (2)
×3	Ba(1)−O(2a)	3.06 (1)	×3	Ba(2)−O(3a)	2.956 (8)
×3	Ba(2a)−O(2a)	2.751 (8)	×3	Ba(3)−O(1)	2.89 (1)
			×3	Ba(3)−O(1′)	2.56 (1)
×3	Ba(2a)−O(3)	2.925 (9)	×6	Ba(3)−O(2)	2.950 (2)
×6	Ba(2a)−O(3a)	2.909 (2)	×3	Ba(3)−O(3)	3.256 (7)
×1	Ba(3a)−O(1)	2.36 (1)			
	Ba(3a)−O(1′)	2.79 (1)			
×2	Ba(3a)−O(1)	2.66 (1)			
×2	Ba(3a)−O(1′)	3.06 (1)			
×2	Ba(3a)−O(2a)	2.938 (2)			
×2	Ba(3a)−O(2a)	3.185 (3)			
×2	Ba(3a)−O(2a)	2.674 (3)			
×1	Ba(3a)−O(3a)	3.302 (7)			
×2	Ba(3a)−O(3a)	3.066 (7)			
×3	Ta(1)−O(3)	2.009 (6)	×3	Ta(2)−O(2)	1.878 (4)
×3	Ta(1)−O(3a)	2.015 (6)	×3	Ta(2)−O(3)	2.110 (5)
×3	Ta(2a)−O(2a)	1.932 (4)			
×3	Ta(2a)−O(3a)	2.137 (6)			
×3	Ta/Mg(3)−O(1)	2.20 (1)	×3	Ta/Mg(3a)−O(1)	1.874 (9)
×3	Ta/Mg(3)−O(1′)	1.87 (1)	×3	Ta/Mg(3a)−O(1′)	2.09 (1)
×3	Ta/Mg(3)−O(2)	2.283 (8)	×3	Ta/Mg(3a)−O(2a)	2.187 (5)

Table 4. Bond Valence Sums (BVS) for $Ba_{10}Mg_{0.25}Ta_{7.9}O_{30}$[a]

atom	assumed oxidation state	BVS[b]	% dev from assumed oxidatn state
Ba(1)	2	1.9	4
Ba(2)	2	2.4	20
Ba(2a)	2	2.5	25
Ba(3)[1]	2	1.8	10
Ba(3)[2]	2	2.6	32
Ba(3)[3]	2	2.1	10
Ba(3a)[1]	2	3.1	54
Ba(3a)[2]	2	2.0	1
Ba(3a)[3]	2	2.7	36
Ta(1)	5	4.7	6
Ta(2)	5	5.2	3
Ta(2a)	5	4.6	8
Mg(3)[1]	2	1.4	31
Mg(3)[2]	2	2.5	25
Mg(3)[3]	2	2.2	12
Ta(3)[1]	5	2.5	49
Ta(3)[2]	5	4.6	8
Ta(3)[3]	5	3.2	17
Mg(3a)[1]	2	2.6	31
Mg(3a)[2]	2	1.8	9
Mg(3a)[3]	2	2.4	20
Ta(3a)[1]	5	4.9	3
Ta(3a)[2]	5	3.4	33
Ta(3a)[3]	5	4.4	13

[a] The split oxygen site occupancies are: 1 − O(1)-1, O(1′)-0; 2−O(1)-0, O(1′)-1; 3−O(1)-066667, O(1′)-033333. [b] BVS (given in valence units) calculated using the VaList program.[30] The calculated BVS for the oxide anions are 1.9 (O1), 1.9 (O1′), 2.0 (O2), 2.0 (O2a), 2.0 (O3), and 2.0 (O3a).

Microwave Dielectric Properties. The synthesis of a material of sufficient purity for compositional and crystallographic characterization still leaves open the requirement to process a ceramic object which can be used in resonator studies to evaluate the dielectric properties. Initial attempts to prepare resonators of $Ba_{10}Mg_{0.25}Ta_{7.9}O_{30}$ with firings of 1550 °C/12 h, 1550 °C/24 h, and 1600 °C/12 h resulted in pellets that did not resonate at microwave frequencies. This was attributed to the low density of the ceramics (85.8%, 84.0%, and 86.4%, respectively). A second trial using new starting material with firings of 1550 °C/12 h and 1550 °C/24 h also gave low density (84.8% and 84.0%) nonresonating pellets. SEM images of the surfaces of these nonresonating ceramics are shown in Figure 7a. Re-firing this second batch of ceramics at higher temperatures and longer times, 1600 °C/24 h and 1650 °C/12 h, increased the densities to 87.1% for both pellets, with the resulting changes to the microstructure seen in the SEM images in Figure 7b.

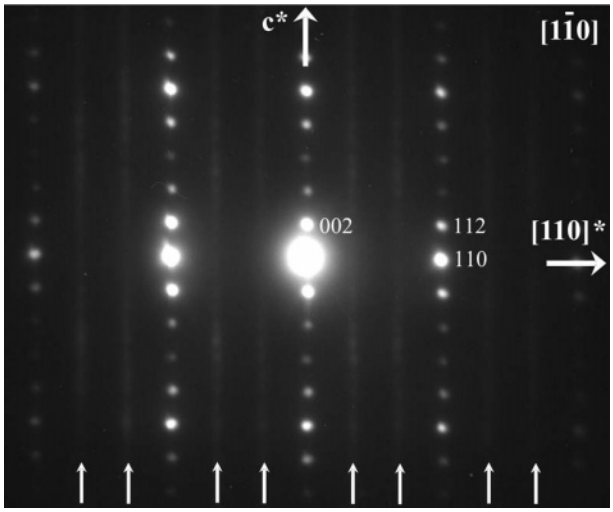

Figure 6. [1−10] zone electron diffraction pattern from $Ba_{10}Mg_{0.25}Ta_{7.5}O_{30}$. The diffuse streaks (marked by white arrows) observed between the rows of Bragg spots are consistent with short-range cation and vacancy ordering.

Table 5. Refinement and Data Collection Details for Powder X-ray and Neutron Diffraction Data for $Ba_8Ta_6ZnO_{24}$[a]

	X-ray	neutron
λ (Å)	1.54059	0.9−5.2 (23−130 ms)
no. of profile points	9599	8397
2θ range (deg), step	8−104, 0.01	⟨168⟩
d-spacing range (Å)	0.81−5.90	0.46−2.6
excluded regions	0	7
χ^2	1.20	2.92
R_E (%)	10.44	4.45
R_{wp} (%)	11.46	7.60
R_p (%)	8.79	6.66

[a] For the two-histogram refinement combined $R_E = 5.94\%$, $R_{wp} = 8.39\%$, $R_p = 8.67$; $\chi^2 = 1.99$ for 74 variables.

Table 6. Structural Parameters for $Ba_8Ta_6ZnO_{24}$ Refined against HRPD Powder Neutron Diffraction and Laboratory X-ray Data[a,b]

atom[c]	multiplicity	*x*/*a*	*y*/*b*	*z*/*c*	*B* (Å^2)
Ba(1)	2	0	0	0.25	0.70(2)
Ba(2)	4	1/3	2/3	0.2362(4)	0.70(2)
Ba(3)	6	0.6569(5)	0	0.6038(5)	0.70(2)
Ba(4)	6	0.3114(4)	0	0.8791(5)	0.70(2)
Ba(5)	6	0.3293(9)	0	0.4885(7)	0.70(2)
Ta(1)[d]	4	1/3	2/3	0.4210(5)	0.39(1)
Zn(2)[e]	4	1/3	2/3	0.0589(6)	0.39(2)
Ta(3)	2	0	0	0.0474(5)	0.39(1)
Ta(4)	6	0.3272(4)	0	0.6765(5)	0.39(1)
Ta(5)	6	0.6643(4)	0	0.8010(5)	0.39(1)
O(1)	6	0.5032(5)	0	0.2388(5)	1.02(9)
O(2)	6	0.1901(4)	*x*	0.8631(5)	0.47(6)
O(3)	6	0.1636(7)	*x*	0.5007(6)	0.56(9)
O(4)	12	0.6679(5)	0.1753(4)	0.4817(5)	1.18(5)
O(5)	12	0.3326(6)	0.1641(5)	0.2426(6)	0.61(4)
O(6)	12	0.6732(5)	0.1624(5)	0.1211(5)	1.07(5)
O(7)	*6*	*0.1571(5)*	*x*	0.1237(5)	0.77(7)
O(8)	12	0.5015(4)	0.3417(4)	0.8572(5)	0.69(5)

[a] Space group: $P6_3cm$. $Z = 3$. Lattice constants: $a = 10.08304(12)$ Å, $c = 19.06594(5)$ Å; $V_c = 1678.69(3)$ Å^3. [b] For the two-histogram refinement combined $R_E = 5.94\%$, $R_{wp} = 8.39\%$, $R_p = 8.67$; $\chi^2 = 1.99$ for 74 variables. [c] Apart from the sites noted, all sites are refined as 100% occupied. [d] Site occupancy equal to 0.853(8)Ta. [e] Site occupancy equal to 0.75Zn + 0.049(8)Ta.

Table 7. Interatomic Distances for $Ba_8Ta_6ZnO_{24}$

		distance, Å			distance, Å
×3	Ba(1)−O(2)	2.885(7)	×3	Ta(1)−O(4)	1.974(9)
×3	Ba(1)−O(7)	2.882(8)	×3	Ta(1)−O(8)	2.098(9)
×6	Ba(1)−O(5)	2.908(7)	×1	Ta(1)−Ta(2)	2.63(1)
×3	Ba(2)−O(1)	2.911(4)	×3	Ta(2)−O(4)	2.17(1)
×3	Ba(2)−O(6)	2.81(1)	×3	Ta(2)−O(6)	2.120(9)
×3	Ba(2)−O(5)	2.920(7)			
×3	Ba(2)−O(8)	2.87(1)			
×1	Ba(3)−O(1)	3.04(1)	×3	Ta(3)−O(3)	1.875(8)
×2	Ba(3)−O(6)	2.901(6)	×3	Ta(3)−O(7)	2.15(1)
×1	Ba(3)−O(3)	2.67(1)			
×2	Ba(3)−O(6)	2.878(5)			
×2	Ba(3)−O(4)	2.89(1)			
×2	Ba(3)−O(7)	3.023(8)			
×2	Ba(3)−O(5)	3.15(1)			
×1	Ba(4)−O(1)	3.26(1)	×1	Ta(4)−O(1)	2.082(9)
×2	Ba(4)−O(5)	3.06(1)	×2	Ta(4)−O(5)	2.09(1)
×2	Ba(4)−O(2)	2.758(5)	×2	Ta(4)−O(6)	1.947(8)
×2	Ba(4)−O(8)	3.061(6)	×1	Ta(4)−O(7)	1.989(9)
×1	Ba(4)−O(3)	2.71(1)			
×2	Ba(4)−O(8)	3.061(6)			
×2	Ba(4)−O(4)	2.71(1)			
×1	Ba(5)−O(2)	2.77(1)	×1	Ta(5)−O(1)	2.064(9)
×2	Ba(5)−O(6)	3.01(1)	×1	Ta(5)−O(2)	1.869(9)
×2	Ba(5)−O(3)	2.89(1)	×2	Ta(5)−O(5)	2.008(9)
×1	Ba(5)−O(7)	3.11(1)	×2	Ta(5)−O(8)	1.961(9)
×2	Ba(5)−O(4)	2.905(4)			
×2	Ba(5)−O(8)	3.01(1)			
×2	Ba(5)−O(4)	2.960(9)			

The identification of suitable conditions for processing the $Ba_8Co_{0.25}Ta_{7.9}O_{30}$ material followed a similar route. Two pellets for dielectric property measurements were made; the first was fired at 1550 °C for 12 h and then for 24 h, the second was fired at 1600 °C for 24 h. The densities of these pellets were 88.9% and 91.7%. They were both found not to resonate. Further firing of both pellets at 1600 °C for a further 24 h increased the densities to 92.1% and 94%, and the dielectric properties were successfully measured.

The dielectric properties were then measured on the densified resonators of both materials. Resonator properties are given in Table 8.

Discussion

The 10-layer phases presented here require synthesis at elevated temperature. This makes the synthesis of the zinc-containing material particularly difficult to control due to reagent volatility and, although it is observed as an impurity in the 8-layer phase, it has not proved possible to isolate it in pure form. Hence the discussion here focuses on the Co and Mg phases which are accessible. The crystal structure refinement of the Mg phase is more straightforward, and hence the structure is discussed based on the refinement of this material.

The composition of $Ba_{10}Ta_{7.9}Mg_{0.25}O_{30}$ differs only very slightly from that of $Ba_5Ta_4O_{15}$—the influence of the Mg^{2+} doping, confirmed by EDS analysis of individual grains, on the structure is however dramatic. $Ba_5Ta_4O_{15}$ adopts a "shift" structure (similar to that in Figure 1b, but with four rather than seven layers of corner sharing octahedra) with two successive h layers in the (cchhc) stacking sequence[20]—the structure has 20% vacancies on the B sites and has these vacancies completely ordered on the central octahedron of the trimer of face-centered octahedra arising from the double h layer. The structure thus consists exclusively of corner-sharing octahedra. The incorporation of 2.5% of magnesium reduces the vacancy loading to 18.5% which would require a small amount of cation (presumably Mg^{2+}) occupancy of the central octahedral site vacant in $Ba_5Ta_4O_{15}$. This would introduce unfavorable repulsions between the octahedral species which could not be overcome by chemical bonding factors. These additional chemical bonding influences are responsible for the existence of trimers of occupied face-sharing octahedra in manganate-based hexagonal perovskites,[21−23] as well as Ba_2NiTeO_6 and Ba_2CoIrO_6.[24,25] The repulsions drive the stabilization of a structure with single h layers in which the Mg^{2+} cations occupy dimers of face-sharing

(20) Shannon, J.; Katz, L. *Acta Crystallogr. B* **1970**, *26*, 102−105.
(21) Fuentes, A. F.; Boulahya, K.; Amador, U. *J. Solid State Chem.* **2004**, *177* (3), 714−720.
(22) Keith, G. M.; Kirk, C. A.; Sarma, K.; Alford, N. M.; Cussen, E. J.; Rosseinsky, M. J.; Sinclair, D. C. *Chem. Mater.* **2004**, *16* (10), 2007−2015.
(23) Wulff, L.; Wedel, B.; Muller-Buschbaum, H. *Zeitschrift Fur Naturforschung B* **1998**, *53* (1), 49−52.
(24) Kohl, P.; Muller, U.; Reinen, D. *Z. Anorg. Allg. Chem.* **1972**, *392* (2), 124.
(25) Vente, J. F.; Battle, P. D. *J. Solid State Chem.* **2000**, *152* (2), 361−373.

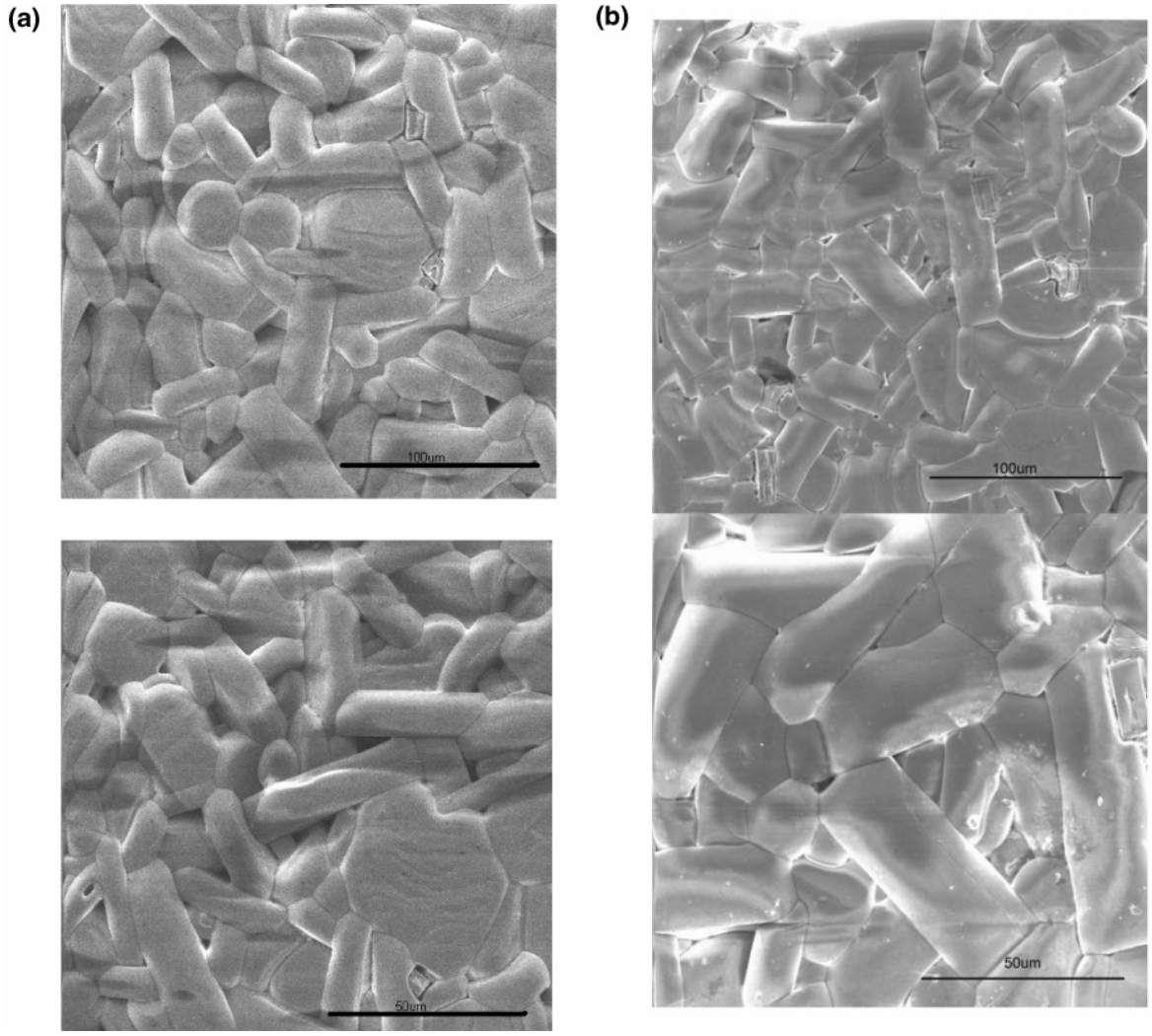

Figure 7. (a) SEM images of nonresonating ceramics of $Ba_{10}Mg_{0.25}Ta_{7.9}O_{30}$ (processed at 1550 °C/12 h, density 84.8%). (b) SEM images of resonating ceramics of $Ba_{10}Mg_{0.25}Ta_{7.9}O_{30}$ (processed at 1550 °C/24 h and 1650 °C/12 h, density 87.1%).

Table 8. Processing Details, Dimensions, Resonator Characteristics, and Dielectric Properties of Resonators Fabricated from the 10-Layer Hexagonal Perovskites $Ba_{10}Mg_{0.25}Ta_{7.9}O_{30}$ and $Ba_{10}Co_{0.25}Ta_{7.9}O_{30}$

composition	processing T(°C)/t (h)	diameter (mm)	height (mm)	density (g cm^{-3})	% of theor. density	f (GHz)	ϵ_r	Q	Qf	τ_f (ppm °C^{-1})
$Ba_{10}Mg_{0.25}Ta_{7.9}O_{30}$	1550/12 and 1600/24	17.22	4.45	6.81	87.1	4.04	28.17	8300	33556	29.1
$Ba_{10}Mg_{0.25}Ta_{7.9}O_{30}$	1550/24 and 1650/12	17.3	4.57	6.81	87.1	4.02	27.79	8350	33585	30.2
$Ba_{10}Co_{0.25}Ta_{7.9}O_{30}$	1550/12, 1550/24 and 1600/24	18.3	4.3	7.2	92.1	3.82	29.74	9550	36495	30.1
$Ba_{10}Co_{0.25}Ta_{7.9}O_{30}$	1600/24 and 1600/24	16.9	5.2	7.35	94.0	3.78	29.74	9700	36693	28.6

octahedra in which they share faces with only one Ta^V species at most. Thus the small dopant concentration produces a dramatic structural change from shift to twin structure. The dielectric properties of $Ba_{10}Ta_{7.9}Mg_{0.25}O_{30}$ and $Ba_{10}Ta_{7.9}Co_{0.25}O_{30}$ are similar to those of $Ba_5Ta_4O_{15}$ which has $\epsilon_r = 28$, Qf = 31 635, and $\tau_f = 12$ ppm/°C.[26]

There are only two other reports of 10-layer hexagonal perovskites detailing the refined structures. In $Ba_5W_3Li_2O_{15}$,[27,28] the refinement of powder neutron data was performed in the space group $P6_3/mmc$ and indicates that W and Li occupy equally the face-sharing octahedral sites in a disordered manner, implying that locally one Li and one W form the face-sharing pair. This example contains no B-site vacancies, and hence the extent of disorder possible in the face-sharing octahedral sites is reduced. The Li cations are also located in the corner-sharing octahedra closest to the face-sharing pair. In the 10-layer phase refined here, there is no evidence for other than complete Ta occupancy of the corner-sharing octahedral sites.

The existence of the face-sharing octahedral units introduced by the h layers in the mixed cubic-hexagonal stacking sequence gives the hexagonal perovskites a much greater ability to absorb cation vacancies on the octahedral sites than the pure cubic sequence. This is because of the enhanced

(26) Kamba, S.; Petzelt, J.; Buixderas, E.; Haubrich, D.; Vanek, P.; Kuzel, P.; Jawahar, I. N.; Sebastian, M. T.; Mohanan, P. *J. Appl. Phys.* **2001**, *89*, 3900−3906.
(27) Jacobson, A. J.; Collins, B. M.; Fender, B. E. F. *Acta Crysallogr. B* **1974**, *30*, 816−819.
(28) Negas, T.; Roth, R. S.; Parker, H. S.; Browser, W. S. *J. Solid State Chem.* **1973**, *8*, 1−13.

repulsion between cations in the face-sharing octahedra and is particularly striking in the shift structures with hh units in the stacking sequence, where an entire layer of octahedral sites (the central octahedron in the trimer of face-sharing octahedra) are left vacant, e.g., in $Ba_5Nb_4O_{15}$. This of course produces much greater complexity in the structural description. In $Ba_{10}Ta_{8-0.8x}Ti_xO_{30}$ ($0.6 \leq x \leq 1.2$), refinement indicates the smaller cell identified here, although in the centric space group $P6_3/mmc$.[29] The lower charge difference between the cations on the B-sites, Ta(V)−Ti(IV) against Ta(V)−Mg(II), results in less preference for cation ordering between the h and c layers in $Ba_{10}Ta_{8-0.8x}Ti_xO_{30}$ e.g at $x = 1.2$ occupation of the corner-sharing sites is 0.9Ta + 0.1Ti, and the face-sharing sites is 0.41Ta + 0.15Ti. In $Ba_{10}Mg_{0.25}Ta_{7.9}O_{30}$, the corner sharing sites are solely occupied by Ta. The centric structure of $Ba_{10}Ta_{7.04}Ti_{1.2}O_{30}$ renders the two face-sharing octahedral sites equivalent and affords two types of corner-sharing octahedra. The first is at the center of the three corner-sharing layers and is symmetrical. The second type is distorted with the central Ta/Ti displaced toward the oxygens that are also part of the face-sharing octahedra. This is driven by the 44% vacancy concentration on the face-sharing site. The Ta/Ti on the face-sharing site are displaced toward the face-sharing oxygens which leads to a short cation−cation distance and considerable anisotropy of the displacement parameters at this site.

There are three corner-sharing sites in the ten layer structure of $Ba_{10}Ta_{7.9}Mg_{0.25}O_{30}$ (Figure 8a). The Ta(1) site at the center of the three layers of corner-sharing sites is intrinsically symmetrical as it is flanked by essentially equivalent neighboring corner-sharing sites (Ta(2) and Ta(2a)), and hence it displays considerably less distortion, with the two distinct sets of three Ta(1)−O bonds being much closer in length than is the case for either of the other two cubic layer sites. As both of the h layer sites are only 55% occupied, the set of short three Ta−O bonds at both Ta(2) and Ta(2a) are made to oxide anions that also form part of the coordination environment of the face-sharing octahedra. The Ta(2)−O(2) bond is shorter than the Ta(2a)−O(2a) one: this can be attributed to the O(2) anion forming part of the site (Ta/Mg(3)) assigned to partial Mg rather than pure Ta occupancy.

There are only two symmetry-inequivalent sites in the hexagonal layers of $Ba_{10}Mg_{0.25}Ta_{7.9}O_{30}$ (Figure 4). The BVS for the face-sharing sites suggest that when Ta/Mg(3) is occupied then so is the O(1′) position and when Ta/Mg(3a) is occupied then so is O(1). Assuming this, then both sites are displaced toward the oxide anions that make up the face of the octahedra that is shared, see Figure 4a. This suggests that locally the cations share faces with vacancies—the Ta/Mg(3) and Ta/Mg(3a) sites have vacancy occupations of 41.05% and 66.45%, respectively. If occupancy of sites within a dimer was correlated, then the cation displacements would be toward the anion face linking with the corner-sharing octahedra. The disorder of cations and vacancies on the h layer sites is not resolved to the same extent by the generation of distinct crystallographic sites as it is in the comparable 8-layer material. The overall B site vacancy concentration in the 10-layer phase is 18.5% of the octahedral sites, compared with 12.5% in the 8-layer phase. As the vacancies are concentrated in the hexagonally stacked layers, it is relevant to consider the level of vacancies within these layers—33% of the octahedral sites in the h layer are empty in the 8-layer phase, while 46% of the h layer sites are vacant in the 10-layer phase.

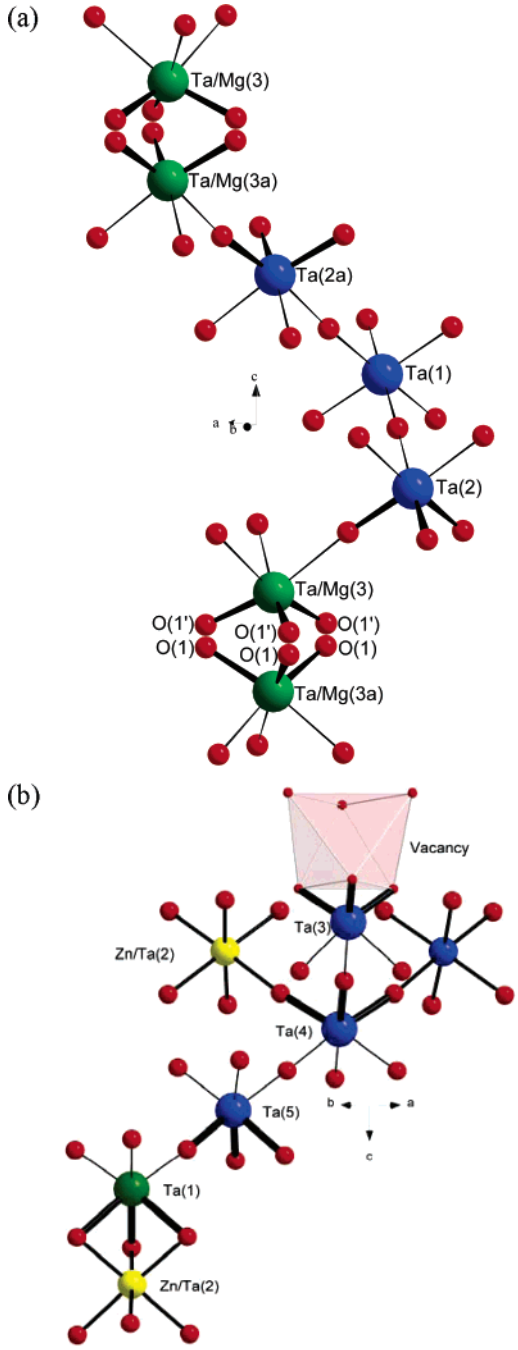

Figure 8. Asymmetric environments of the Ta^V cations in the 8-layer and 10-layer structures are represented by highlighting Ta−O bonds shorter than 2.0 Å as thicker lines are in the structure of (a) $Ba_{10}Mg_{0.25}Ta_{7.9}O_{30}$ and (b) $Ba_8ZnTa_6O_{24}$.

In the 8-layer structure of $Ba_8ZnTa_6O_{24}$, the more extensive long-range site ordering in the h layer allows better identification of the chemical bonding at individual crystal-

(29) Shpanchenko, R. V.; Nistor, L.; van Tendeloo, G.; van Landuyt, J.; Amelinckx, S.; Abakumov, A. M.; Antipov, E. V.; Kovba, L. M. *J. Solid State Chem.* **1995**, *114*, 560−574.

Table 9. Bond Valence Sums (BVS) for $Ba_8Ta_6ZnO_{24}$

atom	assumed oxidatn state	BVS[a]	% dev from assumed oxidatn state
Ba(1)	2	2.3	15
Ba(2)	2	2.4	22
Ba(3)	2	2.1	6
Ba(4)	2	2.3	15
Ba(5)	2	2.0	2
Ta(1)	5	4.4	11
Ta(2)	5	3.3	35
Zn(2)	2	1.8	9
Ta(3)	5	5.0	0
Ta(4)	5	4.6	8
Ta(5)	5	5.1	3

[a] BVS calculated using the VaList program.[30] The calculated BVS for the oxide anions are 1.9 (O1), 2.1 (O2), 2.1 (O3), 1.9 (O4), 1.8 (O5), 2.0 (O6), 1.9 (O7), and 2.1 (O8).

lographic sites (Figure 3b). Considering the sites in the h layer, the Ta(1) site is 85% occupied, and as a result the Ta(1)−O distances reflect less distortion due to multiple bonding than at the fully occupied sites, consistent with this site having the smallest computed Ta bond valence. The Ta(1)−Zn/Ta(2) distance to the neighboring Zn site (75% Zn, 4.9(8)% Ta) of 2.6301(1) Å is acceptable despite the displacement of Ta(1) toward the shared face, compensated by the displacement of Zn/Ta(2) away from it. The predominant occupancy of Zn on this site is confirmed by the bond valence sum analysis shown in Table 9. Ta(3) in the remaining h layer site has a strongly distorted environment, with two sets of three bond lengths of 1.8518(1) Å and 2.1727(1) Å, due to displacement toward the vacant face-sharing octahedral site adjacent to it along *z*. The two corner-shared Ta sites in the c layers, Ta(4) and Ta(5), have quite different geometries due to the widely differing vacancy concentration in the neighboring layers: the Ta(4) site connected to the Zn(2) and Ta(3) face-sharing layer sites is displaced toward the three O atoms bound to these sites and away from those bound to Ta(5) in the c layer below, due to the reduced charge of Zn, and the displacement of Ta(3) toward the vacancy. In contrast Ta(5) makes one very short contact to O(2) to compensate for the cation vacancy of which this anion is part of the coordination sphere. The contacts between Ta(5) and the two anions from the Zn(2) site are shorter than the three contacts to the other face of the octahedra which are bound to Ta(4).

The two layers of face-sharing octahedra consist of a layer of Ta(3) (100% Ta) and Zn(2) (75% Zn, 4.8(9)% Ta) and a layer of vacant sites and Ta(1) (85.3(8)% Ta), hence the distortion at the corner-sharing Ta(5) site is much larger than at Ta(4), as Ta(5) neighbors the highly vacancy-rich layer containing Ta(1). The 100% Ta Ta(3) site shares a face with the vacant site in the h layer, the full occupancy being favored because there is no neighboring face-sharing cation to repel the Ta on the Ta(3) site. Ta(3) thus has the highest calculated bond valence of any of the Ta face-sharing sites, consistent with this occupancy.

The electron diffraction data (Figure 6) for $Ba_{10}Mg_{0.25}Ta_{7.9}O_{30}$ indicate that the X-ray and neutron refinements only probe the average structure at the level of the h layers. The rods of scattering indicate two-dimensional correlations within these layers that do not persist from layer to layer and involve the same basal plane enlargement by a factor of $\sqrt{3}$ that occurs in the case of $Ba_8ZnTa_6O_{24}$. This suggests that the two crystallographically distinct h layer sites in $Ba_{10}Mg_{0.25}Ta_{7.9}O_{30}$ at a local level order further to produce pairing of vacancies and fully occupied Ta sites, with the avoidance of Ta−Ta contacts across shared octahedral faces. The configurational entropy of the B site cations must also be considered when addressing the ordering. At the high temperatures required for synthesis it is likely that the extent of ordering is much lower and only increases during cooling. This may play a role in developing two-dimensional intralayer correlations with less pronounced interlayer correlation observed in the electron diffraction. The different vacancy rate in the h layers in the two cases might be expected to produce differences in the detail of the order. Even at the average level reflected by the subcell 10-layer structure, common features such as displacement of the Ta cations toward the shared face within the h layer and displacement of the c layer cations toward anions shared with the h layer sites indicate similarities with the 8-layer structure.

The crystallography clearly shows that there is less long-range vacancy and cation order within the 10-layer than the 8-layer materials. This enhanced level of positional disorder is amplified by the site splitting of O(1), and the off-center disorder of Ba(3a), which contributes to the noncentric nature of the structure together with the inequivalent Ta occupancy of the face-sharing octahedral sites. The dielectric properties of the 10-layer systems are inferior to those of the 8-layer compound, with Qf being a factor of 2 lower. This can be attributed to the influence of the enhanced static disorder of cation and vacancy location on the losses—this has been extensively studied in site-ordered cubic perovskites such as $Ba_3ZnTa_2O_9$, where extensive B site order has been shown to be a prerequisite for high *Q* materials.[2,4,5] Here the distinction between the h and c layers within the structure already provides a driving force for ordering of cations and vacancies over the octahedral sites, with the vacancies confined to the h layers to prevent direct Ta^V−Ta^V contact at short distance, but more extensive correlation between divalent and pentavalent cations and vacancies, as expressed in the 8-layer structure, is required to minimize losses. The influence of the ordering pattern within one hexagonal layer on that in its neighboring layers is transmitted via the bonding and associated strain fields of the cubic layer cations. The absence of three-dimensional long-range correlations in the 10-layer case may be associated with the enhanced separation between the layers due to the larger size of the intervening cubic block—the effect of the coupling is diluted with distance between the layers and hence the disorder increases with stacking sequence length when the chemistry ($2^+/5^+$/vacancy site ordering) driving the ordering is the same, resulting in enhanced disorder and larger losses in the 10-layer case. New, more powerful ordering motifs will be required for lower loss materials in larger stacking sequence hexagonal perovskites.

(30) Wills, A. S.; Brown, I. D. *Valist*; CEA: France, 1999.

Acknowledgment. We thank EPSRC for Portfolio Partnership support (EPSRC/C511794) and the CCLRC Centre for Materials Physics and Chemistry for partial support of P.M.M.

Supporting Information Available: Crystallographic information for $Ba_{10}Mg_{0.25}Ta_{7.5}O_{30}$ (CIF). This material is available free of charge via the Internet at http://pubs.acs.org.

CM0616477